Nonlocal Electrodynamics in Ultrapure PdCoO$_2$

Graham Baker[1,2] Timothy W. Branch[1,2] J. S. Bobowski[1,2,3] James Day[1,2] Davide Valentinis[4,5]
Mohamed Oudah[1] Philippa McGuinness[6] Seunghyun Khim[6] Piotr Surówka[7,8,9] Yoshiteru Maeno[10,3]
Thomas Scaffidi[11,12] Roderich Moessner[13] Jörg Schmalian[4,5] Andrew P. Mackenzie[6,14] and D. A. Bonn[1,2]

[1]*Stewart Blusson Quantum Matter Institute, University of British Columbia,*
Vancouver, British Columbia, Canada V6T 1Z4
[2]*Department of Physics and Astronomy, University of British Columbia,*
Vancouver, British Columbia, Canada V6T 1Z1
[3]*Department of Physics, Kyoto University, Kyoto 606-8502, Japan*
[4]*Institute for Theory of Condensed Matter, Karlsruhe Institute of Technology, Karlsruhe 76131, Germany*
[5]*Institute for Quantum Materials and Technologies,*
Karlsruhe Institute of Technology, Karlsruhe 76131, Germany
[6]*Max Planck Institute for Chemical Physics of Solids, Nöthnitzer Straße 40, 01187 Dresden, Germany*
[7]*Institute of Theoretical Physics, Wrocław University of Science and Technology, 50-370 Wrocław, Poland*
[8]*Institute for Theoretical Physics, University of Amsterdam, 1090 GL Amsterdam, The Netherlands*
[9]*Dutch Institute for Emergent Phenomena (DIEP), University of Amsterdam,*
1090 GL Amsterdam, The Netherlands
[10]*Toyota Riken-Kyoto University Research Center (TRiKUC), Kyoto 606-8501, Japan*
[11]*Department of Physics and Astronomy, University of California, Irvine, California 92697, USA*
[12]*Department of Physics, University of Toronto, 60 St. George Street, Toronto, Ontario M5S 1A7, Canada*
[13]*Max Planck Institute for the Physics of Complex Systems,*
Nöthnitzer Straße 38, 01187 Dresden, Germany
[14]*Scottish Universities Physics Alliance, School of Physics and Astronomy, University of St Andrews,*
St Andrews KY16 9SS, United Kingdom

The motion of electrons in the vast majority of conductors is diffusive, obeying Ohm's law. However, the recent discovery and growth of high-purity materials with extremely long electronic mean free paths has sparked interest in non-Ohmic alternatives, including viscous and ballistic flow. Although non-Ohmic transport regimes have been discovered across a range of materials—including two-dimensional electron gases, graphene, topological semimetals, and the delafossite metals—determining their nature has proved to be challenging. Here, we report on a new approach to the problem, employing broadband microwave spectroscopy of the delafossite metal PdCoO$_2$ in three distinct sample geometries that would be identical for diffusive transport. The observed differences, which go as far as differing power laws, take advantage of the hexagonal symmetry of the conducting Pd planes of PdCoO$_2$. This permits a particularly elegant symmetry-based diagnostic for nonlocal electrodynamics, with the result favoring predominantly ballistic over strictly hydrodynamic flow. Furthermore, it uncovers a new effect for ballistic electron flow, owing to the highly faceted shape of the hexagonal Fermi surface. We combine our extensive data set with an analysis of the Boltzmann equation to characterize the nonlocal regime in PdCoO$_2$, and we include out-of-plane impurity scattering as a source of apparent momentum-conserving scattering at low temperatures. More broadly, our results highlight the potential of broadband microwave spectroscopy to play a central role in investigating exotic transport regimes in the new generation of ultrahigh-conductivity materials.

I. INTRODUCTION

There has been significant recent interest in unconventional electronic transport regimes in conductors in which a local relationship between the electric current and electric field, as described by Ohm's law, breaks down. In the absence of frequent momentum-relaxing (MR) scattering, nonlocal effects can develop: When momentum-conserving

(MC) scattering is sufficiently frequent, electrons flow collectively as a viscous fluid; when neither form of scattering is frequent, electrons propagate ballistically. While viscous and ballistic effects are conceptually distinct, they can lead to similar experimental signatures [1], making it dangerous to interpret experiments by comparing to theory rooted in one origin or the other. The additional impetus for comparing to theory incorporating both effects comes from the expectation that the hierarchy of scattering rates in most ultrapure materials places them near the ballistic-to-viscous crossover, rather than at an extreme. Adding to the complexity, while early experiments and theories were based on materials with isotropic Fermi surfaces [2,3], a recent theoretical focus has been to extend these ideas to anisotropic systems [4–7]. Many questions remain unresolved, however, and it is vital to extend the range of experimental tools with which to investigate these new transport regimes.

To date, the vast majority of work has been performed in the dc limit because it is difficult to perform broadband ac experiments in the gigahertz region of the spectrum; as we will discuss in more detail below, this is an area in which theory has been ahead of experiment, with predictions for the expected frequency dependencies in different nonlocal regimes but no actual data for comparison. In this paper, we explore this frequency-dependent physics using a unique, bespoke experimental apparatus: a broadband bolometric microwave spectrometer [8]. We report results from a number of ultrapure metals over 1.5 decades of frequency, from 0.6 to 20 GHz. Through measurements on Sr_2RuO_4 and Sn, we verify the predictions for the frequency dependencies of the surface resistance for the classical and anomalous skin effects. Data from the ultrapure delafossite $PdCoO_2$, in contrast, deviate from any previous prediction for the frequency-dependent surface resistance. Analysis of such data requires the construction of a more complete electrodynamic theory of metals than has previously existed, and it allows us to conclude that the $PdCoO_2$ data are due to the combination of a highly anisotropic Fermi surface and a contribution from momentum-conserving scattering. We further show that the appearance of momentum-conserving scattering can be explained by a realistic model of impurity scattering, rather than the usual assumption that it is a sign of electron-electron or electron-phonon scattering.

The paper is organized as follows: After introducing our broadband bolometric technique in Sec. II, we discuss the ac electrodynamics of high-purity metals in Sec. III, and results from Sr_2RuO_4 and Sn in Sec. IV. We then review what is known about nonlocal transport in $PdCoO_2$ in Sec. V, before presenting and analyzing its broadband ac response in Sec. VI. Section VII presents models for scattering that further explain the observed results. We close the paper with Sec. IX, discussing the implications of these results and the future role that ac measurements can play in the study of unconventional transport regimes in metals.

II. MICROWAVE SPECTROSCOPY

Differentiating between nonlocal effects requires transport measurements on length scales comparable to the MR and MC mean free paths, λ_{mr} and λ_{mc}. To date, this has been approached by studying how dc transport properties vary with the dimensions of micro-structured samples. Here, we take a new approach by measuring the ac properties of bulk samples, using the skin effect to impose a *tunable* length scale, the skin depth. In any metal, ac electromagnetic fields decay as they propagate. The result is that the electromagnetic fields—and resulting current density— are confined to a "skin layer" at the surface. A key advantage of ac measurements, in principle, is that this skin depth is frequency dependent: The dc approach necessitates additional fabrication each time sample dimensions are varied, but ac measurements offer the possibility of continuously varying the skin depth. Although conceptually simple, this requires broadband measurement over the microwave range of the spectrum.

Microwave frequencies fall between the range of conventional electrical and optical techniques, presenting a unique challenge for broadband spectroscopy—particularly for high-conductivity samples [8–10]. While reflectivity measurements are commonly used at higher frequencies, at microwave frequencies two difficulties arise: (1) The free-space wavelength becomes comparable to or greater than typical sample dimensions, leading to diffraction, and (2) the reflectivity of high-conductivity metals becomes indistinguishable from unity. At lower frequencies, electrical leads are attached directly to the sample. However, the impedance of high-conductivity samples at microwave frequencies is on the order of milliohms—much lower than typical values of either contact resistance or transmission line impedance.

The most widely adopted technique at microwave frequencies is cavity perturbation, in which a sample's electromagnetic properties are measured via its effect when introduced into a high-Q resonator. Cavity perturbation achieves high sensitivity by amplifying the sample-radiation interaction through repeated reflections. However, the technique suffers the drawback of being at a fixed frequency. As will be discussed in the following section, this eliminates a key means of distinguishing between electrodynamic regimes and necessitates the use of restrictive assumptions when interpreting data.

Here, we report the use of a bespoke technique, giving us the capability of covering the range from 0.6 to 20 GHz continuously [8]. The basis of the technique is a bolometric measurement of the power absorbed by the sample from microwave electromagnetic fields, which is proportional to its surface resistance. Compared to other approaches to spectroscopic measurements at microwave

frequencies [11,12], our technique is uniquely capable of resolving nonlocal effects in high-purity metals as a result of three distinct technical advantages: (1) We achieve high-sensitivity bolometric detection via a miniaturized thermal stage, careful thermometer selection, and home-built signal conditioning electronics. This provides us the sensitivity and dynamic range necessary to cover different skin effect regimes. (2) We use a custom-made transmission line to achieve a contactless, uniform, and well-defined micro-wave field configuration. This permits the separation of anisotropic components and gives us flexibility of measurement geometry—as we shall see, the geometric requirements are even more stringent for nonlocal versus local measurements. (3) We use an *in situ* reference sample to measure the microwave field strength at the sample, eliminating frequency-dependent standing-wave effects and yielding an absolute calibration. Taken together, these technical advantages give us the unprecedented and unmatched ability to measure nonlocal electrodynamics in anisotropic, ultrapure metals.

III. NONLOCAL ELECTRODYNAMICS OF METALS

The skin effect takes several forms depending on the nature of the electron dynamics within the skin layer, each characterized by unique frequency dependence and symmetry constraints of the ac surface resistance. Mathematically, electromagnetic propagation can be conveniently described via a propagator $\mathcal{A}$, which depends on wave vector q and frequency ω:

$$\mathcal{A}_{ij}(\boldsymbol{q}, \omega) = \frac{\mu_0}{i\mu_0\omega\sigma_{ij} + \omega^2/c^2 - q^2}. \tag{1}$$

The poles of $\mathcal{A}$ are solutions to Maxwell's equations, and they give the dispersion relations $q(\omega)$ governing the propagation of electromagnetic modes within the metal. The effect of a metal's conductivity σ is to increase the wave vector and to induce an imaginary component; the skin depth is given by $\delta = 1/\text{Im}(q)$.

In most metals, the relationship between the ac electric field and the induced current density is local—the electric current at a given point in space depends only on the electric field at that same point. This is expressed by Ohm's law:

$$J_i(\boldsymbol{r}, \omega) = \sum_j \sigma_{ij}(\omega)E_j(\boldsymbol{r}, \omega). \tag{2}$$

The reason Ohm's law is valid is that frequent scattering randomizes an electron's momentum on a scale much shorter than the variation of the decaying electric field, giving rise to the classical skin effect (CSE), for which surface resistance is directly related to the local conductivity:

$$R_i(\omega) = \text{Re}\sqrt{\frac{i\mu_0\omega}{\sigma_{ii}(\omega)}}. \tag{3}$$

At low frequency, $R \sim \omega^{1/2}$. The symmetry of R is that of the local conductivity tensor σ, which is set by the crystal system.

However, Ohm's law cannot always be valid: In the absence of MR collisions, an electron's momentum will depend on the entire history of the varying electric field along its trajectory. This can be resolved via a generalized, nonlocal version of Ohm's law using a wave-vector-dependent conductivity:

$$J_i(\boldsymbol{q}, \omega) = \sum_j \sigma_{ij}(\boldsymbol{q}, \omega)E_j(\boldsymbol{q}, \omega). \tag{4}$$

In this case, R is a wave-vector-integrated function of the nonlocal conductivity [13,14], gaining an additional source of anisotropy via the direction of the wave vector $\boldsymbol{q}$ [15]:

$$R_{i,\hat{q}}(\omega) = \text{Re}\left[\frac{i\mu_0\omega}{\pi}\int_{-\infty}^{\infty} dq\,\mathcal{A}_{ii}(\boldsymbol{q}, \omega)\right]. \tag{5}$$

An established instance of nonlocal electrodynamics is the anomalous skin effect (ASE), in which electrons propagate ballistically within the skin layer. The ASE is expected to occur when $\delta \ll \lambda_{\text{mr}}$ [as marked by the red line in Fig. 1(a)], and it is predicted to exhibit a surface resistance that becomes independent of the bulk conductivity and whose magnitude exceeds the CSE expectation [13,16,17]. The ASE has been observed experimentally at low temperature in a select number of high-purity elemental metals [18–21], though always at one fixed frequency. It has also long been predicted that surface resistance follows $\omega^{2/3}$ behavior in the ASE [13,16,17]. To our knowledge, while this frequency dependence has been assumed in the interpretation of fixed-frequency measurements, it has never been measured directly.

Another instance of nonlocal electrodynamics—the viscous skin effect (VSE)—is predicted to occur in an intermediate regime $\sqrt{\lambda_{\text{mr}}\lambda_{\text{mc}}} \ll \delta \ll \lambda_{mc}$ [as shown by the blue and red lines in Fig. 1(b)] and is characterized by $\omega^{3/4}$ behavior [22]. To our knowledge, it has not yet been observed experimentally.

The upper frequency boundary for all of the above skin effects is determined by the onset of the relaxation regime, in which the conductivity leaves the zero-frequency limit. This boundary is given by $\delta = c/\omega_p$, where c is the vacuum speed of light and ω_p is the plasma frequency, as marked by the orange line in Figs. 1(a) and 1(b). For local electrodynamics, this case aligns with the conventional Drude criterion $\omega = \gamma_{\text{mr}}$, shown by the dashed green line in Fig. 1(a).
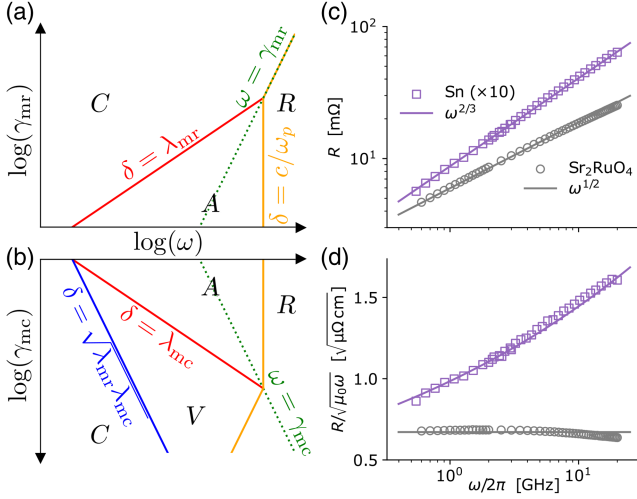
FIG. 1. (a),(b) Predicted skin effect regimes according to conventional theory as a function of frequency ω, momentum-relaxing scattering rate γ_{mr}, and momentum-conserving scattering rate γ_{mc}. (a) Regimes assuming a single scattering rate (i.e., $\gamma_{mc} = \gamma_{mr}$). The transition from classical to anomalous skin effect (represented by C and A, respectively) occurs when the momentum-relaxing mean free path λ_{mr} is longer than the skin depth δ. In this case, electrons propagate ballistically within the skin layer. (b) Regimes allowing for a separate rate for momentum-conserving scattering, taking γ_{mr} to be fixed at its minimum value in panel (a). For sufficiently strong momentum-conserving scattering within the skin layer, a viscous skin effect (represented by V) is predicted to emerge. To our knowledge, this has not yet been experimentally observed. In both panels (a) and (b), the relaxation regime (represented by R) occurs at the highest frequencies, reflecting finite-frequency effects in the conductivity. (c),(d) Spectroscopic surface resistance measurements of Sr_2RuO_4 and Sn. (c) Power-law behavior of $R(\omega)$, indicating that Sr_2RuO_4 exhibits the classical skin effect while Sn exhibits the anomalous skin effect. (d) Dividing R by $\sqrt{\omega}$, which provides a sensitive visual test for deviations from classical $R \sim \sqrt{\omega}$ behavior.

IV. MEASUREMENTS ON Sr_2RuO_4 AND Sn

To set the stage for discussing more complex behavior, we begin by showing spectroscopic measurements of single-crystal Sr_2RuO_4 and polycrystalline Sn in Figs. 1(c) and 1(d). Both measurements were taken using our unique, home-built spectrometer and are slightly above the respective super-conducting transition temperatures. The Sr_2RuO_4 data, taken at 2.6 K, exhibit the $\omega^{1/2}$ behavior expected for the CSE. The magnitude of a CSE fit gives an in-plane resistivity of approximately 50 nΩ cm, consistent with that of the highest-quality samples as measured by conventional dc four-point electrical measurements [23,24]. The slight downward deviation from $\omega^{1/2}$ seen at high frequency is the first hint of a crossover to the relaxation regime [see Fig. 1(a)], and detailed fits shown in Sec. S1C of the Supplemental Material indicate $\gamma_{mr} \sim 680$ GHz [25]; thus, in our spectral range, $\omega < \gamma_{mr}$, and a key condition for observing CSE is satisfied.

The low value of the dc resistivity opens the question of whether the ASE regime would be reached in our frequency range for measurements on Sr_2RuO_4. Although possible in principle, this is a highly anisotropic material, and in the geometry we have chosen for this measurement, the combinations of current direction J and wave vector q avoid the case most likely to show nonlocal effects. In Sec. S1D of the Supplemental Material, we show that the conditions for reaching the ASE regime are not met in this measurement geometry until the THz frequency range [25]. Empirically, this is confirmed by the fact that the only departure from $\omega^{1/2}$ seen here is a deviation downwards at high frequency, due to relaxation effects, rather than the departure upwards to a higher power law as expected for ASE. The influence of measurement geometry will be discussed in more detail when we study measurements of $PdCoO_2$, where we have chosen the crystal orientation most likely to exhibit nonlocal effects.

In contrast to Sr_2RuO_4, the Sn data, taken at 5.0 K, exhibit the $\omega^{2/3}$ behavior expected for the ASE. The magnitude of an ASE fit gives a Fermi velocity of 2.2×10^6 m/s [25], within 20% of the published value of 1.9×10^6 m/s [26]. Because the ASE surface resistance is insensitive to the MR scattering rate, in this case we cannot directly use the information from our fit to compute the expected skin effect boundaries. However, for $\delta < \lambda_{mr}$ to be satisfied over our measurement range implies an upper bound on γ_{mr}, values below which are known to be achievable in high-purity Sn [18,25]. To our knowledge, this is the first-ever spectroscopic measurement of the ASE, confirming the frequency dependence predicted by theory [13,16,17]. Since we are concerned mainly with departures from the CSE, we introduce a plot that emphasizes deviation from its simple $\sqrt{\omega}$ behavior. In Fig. 1(d), we plot the same data sets but rescaled by $\sqrt{\omega}$. For Sr_2RuO_4, the result is quite flat, as expected for the CSE; for Sn, there is a clear upward trend. These measurements highlight our ability to make precise measurements over a broad frequency range, confirming existing theory both in frequency dependence and in absolute magnitude.

V. DC EVIDENCE FOR NONLOCAL TRANSPORT IN $PdCoO_2$

Having established the capability of our spectroscopic technique to differentiate between transport regimes, we now turn our attention to measurements of $PdCoO_2$, whose crystal structure is shown in Fig. 2(a). This material is of considerable interest for ac conductivity measurements because dc studies indicate that it has extremely high purity [27,28] and shows signatures of nonlocal transport. Initial analyses of the dependence of its resistivity on channel width suggested viscous corrections to ballistic transport [29], but the data were analyzed using models previously employed to study non-Ohmic transport in two-dimensional electron gases, in which a circular Fermi surface
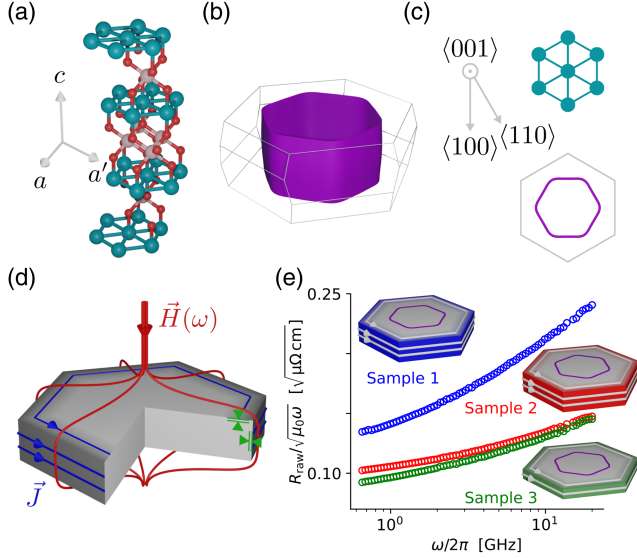
FIG. 2. (a) PdCoO$_2$ crystal structure, belonging to the trigonal crystal system. In this layered structure, the in-plane conductivity is extremely high, but conductivity is much lower along the c axis ($\langle 001 \rangle$). (b) PdCoO$_2$'s hexagonally faceted Fermi surface, as determined via ARPES and quantum oscillations [27]. (c) Looking down along $\langle 001 \rangle$, the in-plane structure is characterized by two Miller indices ($\langle 100 \rangle$ and $\langle 110 \rangle$) rotated 30° with respect to one another, suggesting two ways to orient the sample shape with respect to the hexagonal Fermi surface. (d) Measurement geometry. Samples, which grow naturally as thin platelets, were cut into hexagons to reflect the sixfold rotational symmetry of the crystal structure. A microwave-frequency magnetic field is applied perpendicularly to the plates, thus inducing eddy currents (blue) acting to screen the magnetic field (red) from the interior of the sample. The resulting field strength at the sample's surface (gray shading) is highest on the side faces but also becomes appreciable toward the edges of the top and bottom faces. Because the skin depth is much smaller than the sample dimensions, this gives rise to two separate "skin regions" (indicated by green arrows). In both, current flows in the highly conducting plane ($J \perp \langle 001 \rangle$), and the wave vector is perpendicular to the surface. The measured signal contains a mixture of the two skin regions that depends on the sample's aspect ratio. (e) Raw data. We measured three samples, with two different cut orientations and two different aspect ratios. Sample 1 is cut such that $J \| \langle 100 \rangle$ ($q \| \langle 110 \rangle$) on the side faces; sample 2 is cut such that $J \| \langle 110 \rangle$ ($q \| \langle 100 \rangle$) on the side faces. Varying the aspect ratio between sample 2 and sample 3 enables separation of the contribution from the top and bottom faces, where $q \| \langle 001 \rangle$. All three measurements differ—by symmetry, this can only occur for nonlocal electrodynamics.

was assumed [2,3]. PdCoO$_2$ has the open Fermi surface typical of a quasi-two-dimensional metal [Fig. 2(b)], but the Fermi surface has a faceted, nearly hexagonal cross section [27,30,31]. Although this makes no difference to the local dc transport properties at high temperatures, when a nonlocal dc transport regime is entered at lower temperatures, strong directional effects are seen. Specifically, devices of a given geometry yield different responses depending on their

orientation relative to the Fermi-surface facets [32–34]. To date, the combined role of directional and viscous effects in PdCoO$_2$ has not been analyzed. Furthermore, the origin of the MC scattering needed for viscous effects is a mystery in this material; dc transport measurements on finite channels do not have the temperature dependence expected for hydrodynamic flow due to electron-electron scattering [4]. This background motivated us to investigate whether the ac response of PdCoO$_2$ might be even richer than that predicted for the usual ASE, providing new insight into the physics of PdCoO$_2$.

VI. MEASUREMENTS ON PdCoO$_2$

Our measurements were performed primarily at 2 K so as to match previous nonlocal dc transport studies [29,32–34]. At this temperature, published values imply that the skin depth in our frequency range satisfies $c/\omega_p \ll \delta \ll \lambda_{\mathrm{mr}}$. This is an ideal regime for our investigation; if only momentum-relaxing scattering is present, we would expect to observe the ASE; for sufficient MC scattering, we would be in a position to observe the VSE. Relaxation effects might also come into play, but as shown in Fig. 1(a), the boundary for this is pushed up in frequency by the ASE. Either way, the models used below incorporate relaxation effects as well as the ASE. The faceted Fermi surface of Fig. 2(b) immediately suggests three extremal wave-vector directions for which to perform measurements: $q \| \langle 100 \rangle$, $q \| \langle 110 \rangle$, and $q \| \langle 001 \rangle$. Samples of PdCoO$_2$ grow as platelets, with the $\langle 001 \rangle$ direction perpendicular to the plate and the more highly conducting directions lying in the plane of the plate. In-plane dimensions are around 1 mm, and the thickness is typically tens of microns. To reflect the underlying symmetry of the crystal structure, we cut samples to have hexagonal cross sections, with lateral dimensions of about 0.5 mm [Fig. 2(c)]. We applied a spatially uniform, microwave-frequency magnetic field parallel to the $\langle 001 \rangle$ axis, inducing eddy currents that flow in loops perpendicular to the magnetic field. This method establishes two distinct skin regions: one for currents on the two large hexagonal faces ($J \perp \langle 001 \rangle$, $q \| \langle 001 \rangle$), and the other for currents on the six small rectangular faces ($J \perp \langle 001 \rangle$, $q \perp \langle 001 \rangle$). The currents on the small faces have both q and J lying in the highly conducting plane of this quasi-2D material, maximizing the chance of observing nonlocal effects. The hexagonal cross section of the samples ensures that the wave vectors for each of these six rectangular faces are along symmetry equivalent directions. A measurement of a given sample thus contains a mixture of two distinct surface resistance components— with in- and out-of-plane wave-vector directions—with weights depending on the sample's aspect ratio. Our raw measurements are shown in Fig. 2(d). Sample 1 was such that, on the small faces, $J \| \langle 110 \rangle$ ($q \| \langle 100 \rangle$); sample 2 was cut with $J \| \langle 100 \rangle$ ($q \| \langle 110 \rangle$). The essential difference is the orientation relative to the underlying hexagonally faceted

Fermi surface. Sample 3 was cut with the same orientation as sample 2, but it was thinner, increasing the relative weight of the contribution from the large face ($q\|\langle001\rangle$). With measurements of these three samples, we obtained sufficient information to disentangle the surface resistance components for the three wave-vector directions of interest. However, even without extracting the components, the fact that the three raw measurements differ provides immediate evidence of nonlocal electrodynamics. For all three components, current flows in the highly conducting plane perpendicular to $\langle001\rangle$; for local electrodynamics, the triangular in-plane lattice dictates that the conductivity tensor has no in-plane anisotropy, so all three components —and therefore the three raw measurements that mix them—would be identical. To proceed further, we used electromagnetic simulations to disentangle the surface resistance components, denoted $R_{\langle100\rangle}$, $R_{\langle110\rangle}$, and $R_{\langle001\rangle}$ according to the three distinct wave-vector directions. Details on extracting these components from the raw measurements of the three samples are given in Sec. S3C of the Supplemental Material [25].

The measured surface resistance for the two in-plane wave vectors is shown in Fig. 3(a). Surprisingly, the two orientations exhibit not just different magnitudes but also distinct power-law behaviors. A useful property of the viscosity tensor in a plane with sixfold rotational symmetry provides an elegant avenue for differentiating ballistic and viscous effects: In this setting, as is the case in $PdCoO_2$, the in-plane viscosity tensor is isotropic [35]. This characteristic implies the qualitative insight that the anisotropy in the surface resistance at 2 K for the two orientations cannot be due to purely viscous effects.

With this in mind, we turn to the possible ballistic origin of this effect. The standard theory of the ASE (i.e., ballistic propagation within the skin layer)—Pippard theory [17]—predicts that any orientation should exhibit $R \sim \omega^{2/3}$, with only the prefactor being orientation dependent. Our data are at odds with Pippard theory: While one orientation exhibits behavior close to $\omega^{2/3}$, the other exhibits only a weak deviation from classical behavior. This breakdown of Pippard theory is all the more surprising because—aside from its ubiquity—Pippard theory has previously demonstrated success in describing the behavior of anisotropic Fermi surfaces. Famously, Pippard performed the first-ever experimental determination of a Fermi surface by applying his eponymous theory to measurements of the ASE in Cu, revealing deviation from a spherical Fermi surface [36]. Nonetheless, Pippard theory treats Fermi-surface geometry phenomenologically, and it was originally justified by agreement with more rigorous treatments based on solving the Boltzmann equation for spherical [13] and spheroidal [16] Fermi surfaces.

Clearly, we need to delve deeper. To model our results, we solved the Boltzmann equation using a realistic, three-dimensional parametrization of the Fermi surface of $PdCoO_2$
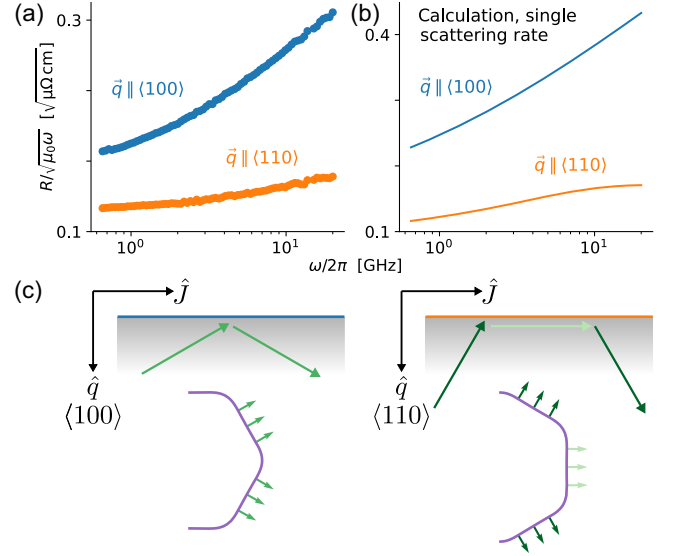
FIG. 3.   (a) Surface resistance data with an in-plane wave vector, obtained by subtracting the $q\|\langle001\rangle$ component from the raw measurements. The different power-law behavior originates from predominantly ballistic propagation within the skin layer coupled with a strongly faceted Fermi surface, as illustrated in panels (b) and (c). (b) Calculated surface resistance based on the experimentally determined Fermi surface, capturing the different power-law behavior of the two orientations. The calculation is for a single relaxation rate, i.e., $\gamma_{mc} = \gamma_{mr}$, and it uses published values with no free parameters [15]. (c) Illustration of ballistic propagation within the skin layer. Left: Two main directions of electron propagation for $\vec{q}\|\langle100\rangle$, both at an angle to the surface. As frequency increases, the skin depth becomes shallower. The electrons spend an increasingly smaller fraction of a mean free path inside the skin layer, leading to an increasing surface resistance—the anomalous skin effect. Right: Three main directions of electron propagation for $\vec{q}\|\langle110\rangle$. Electrons propagating parallel to the sample's surface spend the entirety of a mean free path within the skin layer, regardless of how shallow the skin depth becomes. Often, this is a negligible fraction of the Fermi surface; in $PdCoO_2$, approximately a third of the Fermi surface propagates parallel to the sample's surface. The anomalous skin effect is largely suppressed even when the mean free path is much larger than the skin depth.

based on ARPES and quantum oscillation measurements and assuming a single scattering rate, as described in Appendix A 4 a. As seen in Figs. 3(a) and 3(b), our calculations qualitatively reproduce the difference in power-law behavior between the two orientations. An intuitive explanation for the difference in power laws comes from applying Pippard's "ineffectiveness concept" [17,18] to the Fermi surface of $PdCoO_2$ [Fig. 3(c)]: Only those electrons that spend an entirety of a mean free path within the skin layer are effective at screening electromagnetic fields. As the ratio of mean free path to skin depth increases, electrons spend an increasingly small fraction of a mean free path within the skin layer, so the surface resistance becomes increasingly larger than the classical value. Mathematically,
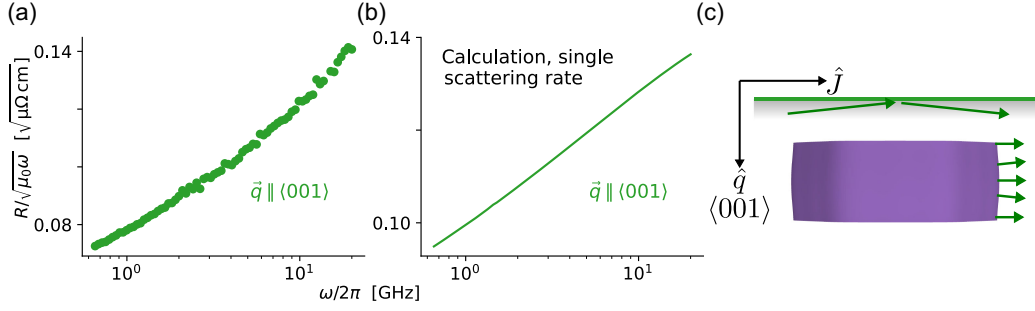
FIG. 4. (a) Surface resistance data with an out-of-plane wave vector, obtained by comparing raw measurements from samples of different thicknesses. The data show upward deviation from classical $R \sim \sqrt{\omega}$ behavior. Because of the high ratio of mean free path to skin depth reached toward the upper end of our frequency range, even the small amount of Fermi-surface warping along k_z is sufficient to produce nonlocal effects. (b) Calculated surface resistance based on the experimentally determined Fermi surface. The calculation is for a single relaxation rate, i.e., $\gamma_{mc} = \gamma_{mr}$, and it uses published values with no free parameters [15]. (c) Illustration of ballistic propagation within the skin layer.

this can be described as an effective mean free path for each state $\mathbf{k}$, which represents that state's contribution to the overall conductivity:

$$\lambda_{\mathbf{k}}^{\text{eff}} = \frac{(\hat{\mathbf{v}}_{\mathbf{k}} \cdot \hat{\mathbf{E}})^2 \lambda_0}{1 + i(\hat{\mathbf{v}}_{\mathbf{k}} \cdot \hat{\mathbf{q}})q\lambda_0}, \tag{6}$$

where λ_0 is the bare mean free path and $\hat{\mathbf{v}}_{\mathbf{k}}$ is the unit velocity vector. (Because the present discussion is focused on purely ballistic effects, here we have taken $\lambda_{mr} = \lambda_{mc} = \lambda_0$). In PdCoO$_2$ in the lower orientation in Fig. 3(c), a third of electrons propagate nearly parallel to the sample's surface, such that $\hat{\mathbf{v}}_{\mathbf{k}} \cdot \hat{\mathbf{q}} = 0$. These electrons remain effective at screening regardless of the ratio of mean free path to skin depth, largely suppressing the increase in surface resistance. Indeed, there have been several theoretical works predicting extreme Fermi-surface geometries for which Pippard theory would break down [37–39]. To our knowledge, the present results represent the first experimental confirmation of these ideas.

The measured surface resistance for the wave vector along the $\langle 001 \rangle$ axis, shown in Fig. 4(a), exhibits a clear deviation from classical $R \sim \sqrt{\omega}$ behavior. The observation of nonlocal electrodynamics in this orientation is surprising: As per the ineffectiveness concept, this means that electrons must be able to propagate in and out of the skin layer within a single mean free path. However, the nearly two-dimensional geometry of the Fermi surface means that, in this orientation, electrons propagate at a shallow angle relative to the skin layer [Fig. 4(c)]. This nearly two-dimensional nature of the electronic transport is indicated by the low-temperature resistivity anisotropy of approximately 1000 [27]. In a perfectly two-dimensional material, the ASE would be completely suppressed in this geometry, so its presence here is a result of the subtle warping of the Fermi surface along k_z, as was resolved by quantum oscillations. This highlights the limitations of a purely

two-dimensional description of transport properties in PdCoO$_2$, and it has implications for dc transport measurements. To date, studies have focused on how resistivity varies when restricting in-plane dimensions; these results imply that size effects will also be present while varying thickness along the $\langle 001 \rangle$ axis. We estimate that the maximum skin depth over our measured frequency range is on the order of 100 nm. This implies that size effects are likely to be especially important to thin films, which have been the subject of recent growth efforts [40–42].

VII. MODELS FOR SCATTERING IN PdCoO$_2$

Although we have identified a ballistic origin for the main features of the three measured surface resistances, the search for the viscous effect leads us to explore a model that allows for arbitrary rates of MR and MC scattering. Combined with a realistic, three-dimensional, Fermi-surface parametrization, these ingredients allow our model to encompass both directional and viscous effects. The model is described in Appendix A 4 b. In Fig. 5, we compare the data for in-plane wave vectors to calculations in which we no longer make our earlier assumption of a single relaxation rate. The only free parameter of these calculations is the MC scattering rate; the MR scattering rate and other material parameters are taken from the literature. As seen in Fig. 5(b), the higher the value of γ_{mc}, the lower the anisotropy between the two surface resistances. This is in accordance with our earlier insight that deep in the viscous regime, symmetry dictates that there should be no anisotropy. The calculations for $\gamma_{mc}/\gamma_{mr} = 1$, shown previously, produce too much anisotropy. For $\gamma_{mc}/\gamma_{mr} = 30$, the isotropic, viscous limit is nearly reached. For intermediate values, a quantitative match to the data is achieved. From this comparison, we determine that $\gamma_{mc} = (7 \pm 3)\gamma_{mr}$ at 2 K.

The fact that our experiments are best matched by $\gamma_{mc} \approx 7\gamma_{mr}$ at 2 K is striking for several reasons. First, it agrees,
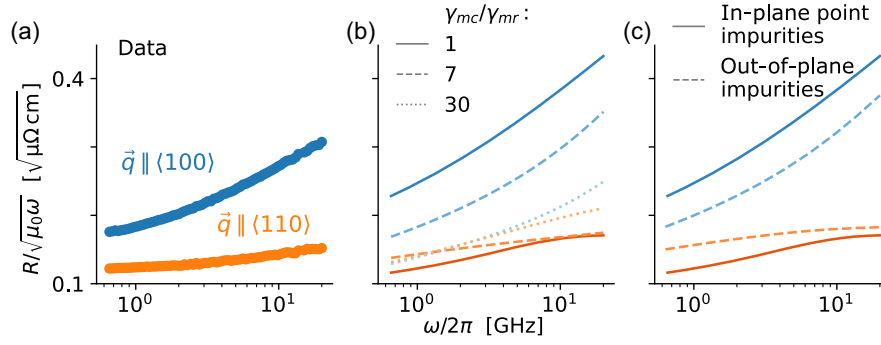
FIG. 5.   Models of scattering in PdCoO$_2$. (a) Experimental surface resistance data at 2 K for in-plane wave vectors $\vec{q}\|\langle 100\rangle$ (blue) and $\vec{q}\|\langle 110\rangle$ (orange), plotted on the same scale as the calculations in panels (b) and (c). (b) Calculated surface resistance within a phenomenological model with separate momentum-relaxing and momentum-conserving scattering rates γ_{mr} and γ_{mc}, following the same color scheme as in panel (a). The model was fitted to the data in panel (a) with γ_{mc} as the only fitting parameter, with γ_{mr} and all other parameters fixed by their literature values. For $\gamma_{mc}/\gamma_{mr} = 1$, corresponding to the conventional relaxation-time approximation, the anisotropy between the two calculated surface resistances is larger than the anisotropy between the two measurements. For $\gamma_{mc}/\gamma_{mr} = 30$, the anisotropy is too small; the two surface resistances are almost equal, as expected deep in the viscous regime. The best fit to the data in panel (a) was achieved for $\gamma_{mc}/\gamma_{mr} = 7$. (c) Calculated surface resistance within a microscopic model of impurity scattering. In-plane impurities give rise to pointlike potentials with isotropic transition probabilities, while out-of-plane, charged impurities give rise to extended potentials that strongly favor forward scattering. The calculation for out-of-plane impurity scattering gives a better match to the data and reproduces the effect of introducing momentum-conserving scattering phenomenologically. This suggests out-of-plane impurity scattering as the origin of the apparent momentum-conserving scattering inferred from the two-scattering-rate model in panel (b).

within experimental errors, with the deduction made in Ref. [29] from the width dependence of dc transport [43]. That dc measurement, however, was performed on a device of unknown orientation relative to the Fermi-surface facets; it was analyzed using the assumption of a circular Fermi-surface cross section, so the agreement may be fortuitous. We believe that the deduction we report here is on a firm footing because orientation and Fermi-surface faceting have been carefully taken into account.

Second, the observation of a contribution from MC scattering raises the question of its source at this low temperature of 2 K. Given that $T \ll T_F$, it is expected that direct electron-electron scattering is negligible, even when taking into account an enhanced cross section due to Fermi-surface faceting [4]. A recent work proposed a phonon-mediated electron-electron interaction as a source of sufficient MC scattering [46], but such a mechanism—indeed, any mechanism invoking electron-electron scattering—would be predominantly MR in PdCoO$_2$ due to Umklapp processes.

The low temperature of our measurements is instead suggestive of an elastic scattering mechanism as the source of the observed MC scattering. Recently, the direct observation of electronic vortices in thin, exfoliated flakes of WTe$_2$ was attributed to small-angle scattering from the top and bottom sample surfaces [47]. While this specific mechanism is not applicable to the present measurements, this indicates that hydrodynamic-like behavior can result from an elastic scattering mechanism.

Here, we consider electronic scattering from bulk impurities. Impurities are often considered to act as short-range

potentials, which, in the zero-range limit, gives rise to isotropic transition probabilities and scattering described by a single rate. However, the layered nature of PdCoO$_2$, in which electrical conduction is dominated by the Pd planes, offers a different possibility. While in-plane defects give rise to conventional short-range potentials, charged defects in the CoO$_2$ layers instead give rise to spatially extended potentials. The greater the spatial extent of the potential, the narrower its extent in reciprocal space, favoring scattering with small momentum transfer. Therefore, scattering of electrons by out-of-plane impurities gives rise to predominantly forward scattering, which is inefficient at relaxing momentum. It has been established that the defect density in the Pd layers is extremely low [28], so out-of-plane impurities likely dominate.

To test the hypothesis that the observed momentum-conserving scattering comes from out-of-plane impurities, we develop a model that assumes that the out-of-plane impurities reside at the Co atom sites, and we calculate the screened potential in the Pd planes. Going beyond our previous single- and dual-rate relaxation-time approximations (RTAs), we solve the Boltzmann equation using the full, microscopic collision operator accounting for the scattering probabilities between all states on the Fermi surface. Full details of the calculation are given in Appendix A 4 c. Fig. 5(c) shows that the calculation for out-of-plane, charged impurities provides a better match to the data than that for in-plane impurities. More importantly, it provides a physical mechanism that reproduces the decreased anisotropy that one gets by invoking MC scattering.
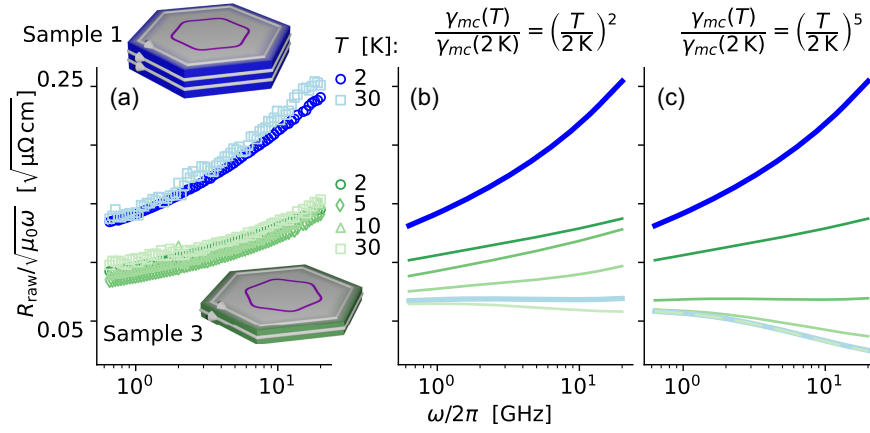
FIG. 6.   (a) Temperature-dependent raw surface resistance data for PdCoO$_2$. (b) Calculations assuming $\gamma_{\mathrm{mc}}(T) = (T/2\ \mathrm{K})^2 \gamma_{\mathrm{mc}}(2\ \mathrm{K})$, as would be expected if $\gamma_{\mathrm{mc}}(2\ \mathrm{K})$ were dominated by electron-electron scattering [48]. (c) Calculations assuming $\gamma_{\mathrm{mc}}(T) = (T/2\ \mathrm{K})^5 \gamma_{\mathrm{mc}}(2\ \mathrm{K})$, as would be expected if $\gamma_{\mathrm{mc}}(2\ \mathrm{K})$ were dominated by electron-phonon scattering [49]. The color scheme in panels (b) and (c) follows that from panel (a). The data in panel (a) do not follow the trend of the calculations in panel (b) or (c) but are instead nearly temperature independent, as expected if $\gamma_{\mathrm{mc}}(2\ \mathrm{K})$ were dominated by electron-impurity scattering.

A test of the impurity-based scenario is to look at temperature-dependent data. Between 2 K and 30 K, the in-plane resistivity shows that the MR scattering rate is dominated by impurity scattering [27]. An electron-impurity contribution to the MC scattering rate is expected to be temperature independent. On the other hand, an electron-electron contribution is expected to vary as T^2 [48]. An electron-phonon contribution, which can, in principle, occur due to phonon drag [29,49,50], is expected to vary as T^5 [49].

In Fig. 6, we show temperature-dependent raw data up to 30 K in addition to the 2-K data shown earlier. We compare the data with calculations of the temperature dependence expected if the MC scattering rate found at 2 K were dominated by either electron-electron or electron-phonon scattering (details of the calculations are given in Sec. S4 of the Supplemental Material [25]). As temperature rises, the increasing MC scattering rate rapidly pushes the calculated spectra downward as the crossover frequency from the local regime is pushed higher [cf. Fig. 1(b)]. In contrast, the data show little temperature dependence, ruling out both of these scenarios.

Scattering by out-of-plane impurities offers insights into other aspects of PdCoO$_2$ and likely other ultrahigh-conductivity materials as well. The ratio of the transport scattering rate (as inferred from resistivity) to the single-particle scattering rate (as inferred from quantum oscillations) is particularly extreme in PdCoO$_2$ as compared to conventional metals [27,51]. In Ref. [29], it was argued that this fact provides additional evidence for the presence of MC scattering. In fact, scattering from out-of-plane impurities has already been established as the source of the small low-temperature ratio of transport to single-particle scattering rates both in GaAs-based two-dimensional electron gases [52,53] and in graphene [54,55]. Our model can be used to calculate this ratio for PdCoO$_2$: Using the same parameters as

in the surface resistance calculation in Fig. 5(c), we calculate a ratio of 4%. Experimentally, below 4 K where quantum oscillations become visible, the ratio is found to be approximately 3% [27].

Actually, the presence of out-of-plane impurities may be related to the origin of ultrahigh conductivity itself—an important question in PdCoO$_2$, being among the highest-conductivity materials known. Because they are inefficient at relaxing momentum, the concentration of out-of-plane impurities corresponding to a given rate of MR scattering is much higher than the concentration of short-range impurities needed to reach that same rate. Reference [28] posed the question of whether ultrahigh conductivity in PdCoO$_2$ was a result of low impurity concentration or suppressed backscattering. The answer may be a combination of both: While the ultrahigh conductivity of PdCoO$_2$ relies on an extremely low concentration of defects in the Pd planes, as established to be the case in Ref. [28], our model implies it is rather insensitive to a large concentration of impurities in the CoO$_2$ layers, leading to predominantly forward scattering. The physics of out-of-plane impurities may be relevant to the low-temperature properties of many layered materials: Ultrahigh conductivity can be achieved when out-of-plane impurities are the dominant scattering mechanism [56]; in turn, the nontrivial consequences of out-of-plane impurity scattering are manifested in nonlocal transport properties, which are observable as a result of ultrahigh conductivity.

VIII. DISCUSSION

It is important to discuss similarities and differences between the scenario developed above and the use of a two-rate model in conventional hydrodynamics. While electronic transport properties depend, in principle, on the

transition rates between all pairs of electronic states, as induced by microscopic interactions, in the vast majority of materials it is possible to make the drastic approximation of describing the effect of all scattering by a single rate. The full microscopic description of scattering involves a collision matrix C whose elements $C_{kk'}$ describe the transition rate from state k to state k'. The RTA is the ubiquitous assumption that this entire collision matrix can be replaced by a single scattering rate.

For bulk transport, the RTA is justified, with a caveat. Using the full collision matrix, the bulk conductivity is given by $\sigma_{xx} = e^2 \langle v_x | C^{-1} | v_x \rangle$ [58]. This formula can be rewritten in the conventional Drude form in terms of a single scattering rate, $\sigma_{xx} = e^2 \langle v_x | v_x \rangle / \gamma_{\mathrm{tr}}$, so long as the transport scattering rate is understood as $1/\gamma_{\mathrm{tr}} \equiv \langle v_x | C^{-1} | v_x \rangle / \langle v_x | v_x \rangle$. It is recognized that this rate is a weighted average over the elements of C, which can, in general, differ from the single-particle scattering rate $\gamma_k^{\mathrm{sp}} = C_{kk}$.

For nonlocal transport, the conductivity is given by $\sigma_{xx}(q_y) = e^2 \langle v_x | [C + i q_y v_y]^{-1} | v_x \rangle$. Unlike bulk transport, the nonlocal conductivity cannot be written in terms of a single scattering rate. As q_y is varied (in our case, by varying the skin depth; in dc measurements, by varying device dimensions), the measured conductivity corresponds to a changing weighted average over the collision matrix C.

The traditional proposal of a two-rate model with which we compared our data above, with separate rates for momentum-relaxing and momentum-conserving scattering, is usually motivated by capturing the onset of a hydrodynamic regime in the limit $\gamma_{\mathrm{mc}} \gg \gamma_{\mathrm{mr}}$. In this picture, the two rates arise from two separate scattering mechanisms—one entirely efficient at relaxing momentum and the other conserving momentum completely. The momentum-conserving scattering is associated with inelastic electron-electron processes that also ensure local equilibrium on the scale of λ_{mc}.

However, the two-rate model would be expected to describe data better than the conventional (single) RTA in any nonlocal transport measurement in which scattering is characterized by more than one rate, even if the additional rates are unconnected with local equilibration. Indeed, any scattering mechanism with a transition probability that depends on the scattering vector between initial and final states can, in principle, give rise to a hierarchy of associated rates. We believe this case is applicable to our own data, with out-of-plane impurities providing spatially extended potentials and therefore a scattering vector-dependent transition probability. Therefore, a key result of our analysis is that we have observed scattering beyond the RTA in PdCoO$_2$. It is not possible to reproduce our data by invoking a single scattering rate—the transport rate sets the overall magnitude of the surface resistance while the presence of shorter timescales influences its shape and anisotropy. This regime is intermediate to the Ohmic and ballistic regimes but distinct from the conventional hydrodynamic regime. As ultrahigh-conductivity materials have become available, enabling nonlocal transport measurements, a common approach has been to analyze data in terms of the two-rate model. If the two-rate model performs better than a single-rate model, it is interpreted in terms of hydrodynamics. However, especially when the two rates are not well separated, it need not involve standard hydrodynamics at all, even when experimental data show what were previously thought of as its hallmarks [47].

Independently from the search for electron hydrodynamics, obtaining experimental information about microscopic scattering processes, beyond that available from bulk resistivity measurements, is of widespread interest in condensed matter physics. This usually comes via arduous comparisons of the scattering rates inferred from multiple techniques, e.g., comparing electrical with thermal and single-particle scattering rates. The possibility of having a tunable sensitivity to microscopic scattering processes within a single nonlocal experiment—as we have demonstrated here—represents an exciting advancement offering a breadth of novel opportunities.

IX. OUTLOOK

The results presented in this paper have future implications both for understanding the physics of PdCoO$_2$ and for the broader field of nonlocal effects in ultraclean metals. For the first time, we have combined experiment and analysis to investigate the combined effects of scattering beyond the RTA and Fermi-surface anisotropy—including both the effect of in-plane faceting and out-of-plane warping. In PdCoO$_2$ and other delafossites, the existence of a Boltzmann transport code capable of working with realistic Fermi-surface parametrizations will enable further in-depth investigation of the balance between MC and MR scattering in both the ac and dc regimes. By extending the range of frequencies over which there is information to 20 GHz and showing the unconventional frequency dependencies revealed in our measurements, we have provided a stringent test for this analysis model. Its ability to reproduce those frequency dependencies gives us more confidence in its correctness (and in the assumptions on which it is based) than could ever be achieved from dc data alone. While Refs. [32–34] showed that Fermi-surface geometry and orientation can have an effect on nonlocal transport, here we have shown that they can go as far as modifying the power-law relationship between transport properties and an imposed, extrinsic length scale. Both in the skin effect and the size effect in narrow channels, these power laws are often taken as an unambiguous means to differentiate between diffusive, viscous, and ballistic transport. Our findings highlight that Fermi-surface geometry and orientation can act as confounding factors when differentiating between transport regimes. Here, we observed that predominantly ballistic electron dynamics lead to behavior close to the expected $\omega^{2/3}$

dependence in one orientation, but in another orientation, they lead to behavior much closer to the $\omega^{1/2}$ dependence typically associated with diffusive dynamics. This indicates that in dc experiments, orientation-dependent differences from the canonical quadratic relationship between conductance and width in the ballistic regime are likely to be seen in width-restricted channel experiments performed in carefully oriented channels. The success of our ac Boltzmann transport theory in turn enables extension of this kind of study to other ultrahigh-conductivity materials with known Fermi surfaces and prediction of the nonlocal ac transport effects likely to be found in them.

Experimentally, we have demonstrated the utility of broadband microwave spectroscopy in the investigation of nonlocal electrodynamics. While the foundational measurements of the ASE were performed at fixed frequencies [18–20,36], in the present work, continuous-frequency measurements were critical to the interpretation of our results: in particular, in identifying a ballistic- rather than viscous-dominated regime, and in revealing the predicted breakdown of Pippard theory as a result of a strongly faceted Fermi surface. These effects are also technologically relevant, as future applications of ultrahigh-conductivity materials are likely to operate at gigahertz frequencies. The ASE is known to limit the conductance of interconnects in integrated circuits when operated at these high frequencies [59]. The present results demonstrate that conductance can be improved by aligning interconnects along a direction for which the ASE is suppressed. Finally, to our knowledge, our findings represent the first experimental observation of the ASE outside of elemental metals, suggesting experimental opportunities among new-generation ultrahigh-conductivity materials. The interplay of frequency, scattering rates, carrier density, and Fermi-surface geometry gives rise to a rich phenomenological landscape for nonlocal electrodynamics, particularly in the microwave and terahertz range—which, to date, remains largely unexplored [44,60–64].

APPENDIX: SURFACE RESISTANCE CALCULATIONS

1. Surface resistance

The quantity we measured experimentally was surface resistance R. For specular scattering of electrons at the sample's surface, surface impedance is given by [13]

$$R_{i,j} = \text{Re}\left\{\frac{i\mu_0\omega}{\pi}\int_{-\infty}^{\infty}dq\,\mathcal{A}_{ii}(q_j,\omega)\right\} \quad \text{(A1)}$$

while for diffuse scattering, it is given by [14]

$$R_{i,j} = \text{Re}\left\{i\mu_0\omega\pi\left[\int_0^{\infty}dq\ln\left(\frac{1}{q^2\mathcal{A}_{ii}(q_j,\omega)}\right)\right]^{-1}\right\} \quad \text{(A2)}$$

with

$$\mathcal{A}_{ii}(q_j,\omega) = \frac{1}{i\mu_0\omega\sigma_{ii}(q_j,\omega)+\omega^2/c^2-q^2} \quad \text{(A3)}$$

and where $\sigma_{ii}(q_j,\omega)$ is the nonlocal transverse conductivity. Diffuse boundary scattering was assumed for all calculations in the main text.

2. Nonlocal conductivity

The nonlocal conductivity was calculated via the Boltzmann equation. In the presence of an electric field $\boldsymbol{E} = E_i e^{i(q_j r_j-\omega t)}\hat{\imath}$, the linearized electronic Boltzmann equation is given by

$$[\hat{C}+i(v_{kj}q_j-\omega)]\psi_k(q_j,\omega) = -eE_i(q_j,\omega)v_{ki}. \quad \text{(A4)}$$

Here, we have expanded the distribution function f_k as

$$f_k = f_0 + \left(-\frac{\partial f}{\partial\mathcal{E}_k}\right)\psi_k, \quad \text{(A5)}$$

where f_0 is the equilibrium Fermi-Dirac distribution function and we have taken $\psi_k(r_j,t) = \psi_k(q_j,\omega)e^{i(q_j r_j-\omega t)}$. The electronic group velocity $\boldsymbol{v}_k$ is given by $\boldsymbol{v}_k = (1/\hbar)\nabla_k\mathcal{E}_k$, where $\mathcal{E}_k$ is the electronic dispersion. Finally, the linearized collision operator $\hat{C}$ is defined by $\hat{C}\psi_k = \sum_{k'}C_{kk'}\psi_{k'}$, with

$$C_{kk'} \equiv \frac{1}{(-\partial f_0/\partial \mathcal{E}_k)} \frac{\delta \mathcal{C}_k}{\delta \psi_{k'}}, \tag{A6}$$

where $\mathcal{C}_k$ is the full Boltzmann collision operator. In Appendix A 4, we consider three different models for $\hat{C}$. With $\hat{C}$ specified, the Boltzmann equation is solved for f_k, and the conductivity is found as

$$\sigma_{ii}(q_j, \omega) = \frac{J_i(q_j, \omega)}{E_i(q_j, \omega)}, \tag{A7}$$

where the current is given by

$$J_i(q_j, \omega) = -2e \sum_k v_{ki} f_k(q_j, \omega). \tag{A8}$$

3. Fermi-surface parametrization

The conductivities in Appendix A 4 involve sums of the form $\sum_k (-\partial f_0/\partial \mathcal{E}_k) F_k$ for some function F_k. Here, we describe how the electronic dispersion of PdCoO$_2$ is incorporated into these sums. For PdCoO$_2$, $T_F \approx 30\,000$ K, and $T \ll T_F$ for all temperatures of interest. In this case, $(-\partial f_0/\partial \mathcal{E}_k) \approx \delta(\mathcal{E}_k - \mathcal{E}_F)$, so

$$\sum_k \left(-\frac{\partial f_0}{\partial \mathcal{E}}\right) F_k \approx \frac{1}{(2\pi)^3} \int_{\mathcal{S}(\mathcal{E}_F)} dS \frac{F_k}{\hbar v_k}, \tag{A9}$$

where $\mathcal{S}(\mathcal{E}_F)$ denotes the Fermi surface. For a Fermi surface parametrized by the Fermi vector $k_F(g, h)$ with $g \in \{g_1, g_2\}$ and $h \in \{h_1, h_2\}$, we define the vector n by

$$n(g, h) \equiv \frac{\partial k_F(g, h)}{\partial g} \times \frac{\partial k_F(g, h)}{\partial h} \tag{A10}$$

such that

$$\int_{\mathcal{S}(\mathcal{E}_F)} \frac{dS}{\hbar v_k} F_k = \int_{g_1}^{g_2} dg \int_{h_1}^{h_2} dh \frac{n(g, h)}{\hbar v(g, h)} F(g, h), \tag{A11}$$

where $n(g, h) \equiv |n(g, h)|$. Furthermore, $\hat{n}(g, h) \equiv n(g, h)/n(g, h)$ describes the unit vector in the direction of the Fermi velocity (i.e., perpendicular to the Fermi surface). For PdCoO$_2$, we used the Fermi-surface parametrization from Hicks *et al.* [27]:

$$k_F(\phi, k_z) = \rho(\phi - \phi_0, k_z)[\cos\phi \hat{i} + \sin\phi \hat{j}] + k_z \hat{k}, \tag{A12}$$

where

TABLE I. Harmonics for parametrization of the Fermi surface of PdCoO$_2$ from Hicks *et al.* [27].

μ	ν	$k_{\mu,\nu}$ (Å^{-1})
0	0	0.9538
6	0	0.040
12	0	0.007
0	1	0.0107
0	2	−0.009
3	1	0.0010

$$\rho(\phi - \phi_0, k_z) = \sum_{\mu,\nu} k_{\mu\nu} \cos[\mu(\phi - \phi_0)]$$
$$\times \begin{cases} \sin[\nu d k_z] & k_{31} \\ \cos[\nu d k_z] & \text{otherwise,} \end{cases} \tag{A13}$$

with $d = c/3$, where $c = 17.743$ Å and with the Fermi-surface harmonics listed in Table I. Here, $\phi \in \{0, 2\pi\}$, $k_z \in \{-\pi/d, \pi/d\}$, and the angle ϕ_0 sets the in-plane rotation of the Fermi surface relative to the coordinate system. For simplicity, we assume that the magnitude of the Fermi velocity is constant on the Fermi surface:

$$v_k = v_F \hat{n} \tag{A14}$$

for $k \in \mathcal{S}(\mathcal{E}_F)$.

4. Models of scattering

Here, we describe the three models for the collision operator that we used to analyze our data.

a. Single relaxation-time approximation

The "single relaxation-time approximation" was used for the calculations shown in Figs. 3(b) and 4(b). It consists of replacing the collision operator by a single scattering rate:

$$\hat{C} = \gamma_{\mathrm{mr}}. \tag{A15}$$

In this case,

$$\sigma_{ii}(q_j, \omega) = 2e^2 \sum_k \left(-\frac{\partial f_0}{\partial \mathcal{E}_k}\right) \frac{v_{ki}^2}{\gamma_{\mathrm{mr}} - i\omega + i v_{kj} q_j}. \tag{A16}$$

For our calculations, we used the value $\gamma_{\mathrm{mr}} = 35$ GHz. This was inferred from experimentally determined quantities using $\gamma_{\mathrm{mr}} = \epsilon_0 \omega_{p,ab}^2 \rho_{ab}$, with the residual resistivity $\rho_{ab} = 7.5$ nΩ cm and the plasma frequency $\omega_{p,ab} = 7.2 \times 10^{15}$ Hz [27].

b. Dual relaxation-time approximation

The "dual relaxation-time approximation" was used for the calculations shown in Figs. 5(b), 6(b), and 6(c).

Its purpose is to capture the scenario in which momentum is slowly relaxed at a rate γ_{mr}, while other scattering processes occur at a faster rate γ_{mc}. Introducing the inner product [44,45]

$$\langle a|b \rangle = \sum_k \left(-\frac{\partial f_0}{\partial \mathcal{E}_k} \right) a_k^* b_k, \qquad (A17)$$

we constructed the collision operator in the basis of its real-valued eigenmodes, which satisfy

$$\hat{C}|\chi_m\rangle = \gamma_m |\chi_m\rangle. \qquad (A18)$$

Conservation of electron number implies an eigenmode $|\chi_0\rangle = |1\rangle$ with eigenvalue $\gamma_0 = 0$. We assume that the eigenmodes also include

$$|\chi_{1\alpha}\rangle = |p_\alpha\rangle \qquad (A19)$$

with eigenvalue γ_{mr}, where p_α represents the component of momentum p along the $\hat{\alpha}$ direction [65]. Finally, we assume that all other eigenmodes have eigenvalue γ_{mc}. The completeness of the eigenbasis then allows us to write the collision operator without having to specify the remaining eigenmodes:

$$\hat{C} = \gamma_{\mathrm{mc}} \left(1 - \frac{|\chi_0\rangle\langle\chi_0|}{\langle\chi_0|\chi_0\rangle} \right) - (\gamma_{\mathrm{mc}} - \gamma_{\mathrm{mr}}) \sum_\alpha \frac{|\chi_{1\alpha}\rangle\langle\chi_{1\alpha}|}{\langle\chi_{1\alpha}|\chi_{1\alpha}\rangle}. \qquad (A20)$$

The solution to the Boltzmann equation is significantly simplified if the system contains three mirror symmetry planes. While this symmetry is weakly broken in PdCoO$_2$ by k_{31}, here we made the approximation that $k_{31} = 0$ to take advantage of this simplification. In this case, the conductivity is given by [44,45]

$$\sigma_{ii}(q_j, \omega) = \langle v_i | M_j | v_i \rangle + \frac{\gamma_{\mathrm{mc}} - \gamma_{\mathrm{mr}}}{\langle p_i | p_i \rangle} \langle v_i | M_j | p_i \rangle^2$$

$$\times \left[1 - \frac{\gamma_{\mathrm{mc}} - \gamma_{\mathrm{mr}}}{\langle p_i | p_i \rangle} \langle p_i | M_j | p_i \rangle \right]^{-1}, \qquad (A21)$$

where

$$M_j \equiv \frac{1}{\gamma_{\mathrm{mc}} + i(v_{kj}q_j - \omega)}. \qquad (A22)$$

We used $\gamma_{\mathrm{mr}} = 35$ GHz as before and treated γ_{mc} as a free parameter.

c. Model for out-of-plane impurities

This model was used for the calculations in Fig. 5(c), and it is based on a microscopic model of the full collision operator. Here, the calculation was performed by

discretizing the Fermi surface and recognizing eq. (A4) as a system of linear equations

$$\sum_{k'} G_{kk'} \psi_{k'}(q_j, \omega) = -eE_i(q_j, \omega) v_{ki}, \qquad (A23)$$

with

$$G_{kk'} \equiv C_{kk'} + i(v_{kj}q_j - \omega)\delta_{kk'}. \qquad (A24)$$

The conductivity was calculated by a numerical solution of this system of linear equations:

$$\sigma_{ii}(q_j, \omega) = 2e^2 \sum_{kk'} \left(-\frac{\partial f_0}{\partial \mathcal{E}_k} \right) v_{ki} G_{kk'}^{-1} v_{k'i}. \qquad (A25)$$

For simplicity, here we used a two-dimensional approximation, using the Fermi-surface harmonics in Table I with $k_{\mu\nu} = 0$ for $\nu \neq 0$. The collision operator is related to the equilibrium transition probability $P_{kk'}$ by

$$C_{kk'} = \frac{1}{f_0(\mathcal{E}_k)[1 - f_0(\mathcal{E}_k)]} \left(-P_{kk'} + \sum_{k''} P_{kk''} \delta_{kk'} \right). \qquad (A26)$$

For scattering of electrons from dilute, randomly distributed impurities, $P_{kk'}$ is given by

$$P_{kk'} = \frac{2\pi}{\hbar} n_i |V_{kk'}|^2 f_0(\mathcal{E}_k)[1 - f_0(\mathcal{E}_{k'})]\delta(\mathcal{E}_k - \mathcal{E}_{k'}), \qquad (A27)$$

where n_i is the concentration of impurities. For $V_{kk'}$, we used the screened potential for an impurity with charge Q_i situated at a height z_i from a two-dimensional conducting plane [66]:

$$V_{kk'} = \frac{Q_i}{\epsilon_b} \frac{\exp(-|k - k'|z_i)}{|k - k'| + \kappa}, \qquad (A28)$$

where ϵ_b is the background dielectric constant and κ is the two-dimensional Thomas-Fermi wave vector given by

$$\kappa = \frac{2\pi e^2}{\epsilon_b} \frac{dn}{d\mu}. \qquad (A29)$$

For $T \ll T_F$, $dn/d\mu \approx \mathcal{D}(\mathcal{E}_F)$, where $\mathcal{D}(\mathcal{E}_F)$ is the two-dimensional density of states at the Fermi energy, given by

$$\mathcal{D}(\mathcal{E}_F) = \frac{2}{(2\pi)^2} \int_{\mathcal{S}(\mathcal{E}_F)} \frac{dS}{\hbar v_k}. \qquad (A30)$$

Using our Fermi-surface parametrization and the value $\epsilon_b = 50\epsilon_0$ [67], we found that $\kappa = 1.42$ Å^{-1}. For z_i, we used a value of 2.96 Å, the distance between the Pd planes and the nearest Co atom. The factor $n_i|Q_i|^2$ was found using the

experimentally determined residual in-plane resistivity $\rho_{ab} = 7.5$ nΩ cm [27]. To compare transport and single-particle scattering rates, we used the formula [68]

$$\gamma[w_{\boldsymbol{k}\boldsymbol{k}'}] = N(0) \frac{\frac{1}{k_B T}\sum_{\boldsymbol{k}\boldsymbol{k}'} P_{\boldsymbol{k}\boldsymbol{k}'} w_{\boldsymbol{k}\boldsymbol{k}'}}{\sum_{\boldsymbol{k}\boldsymbol{k}'} w_{\boldsymbol{k}\boldsymbol{k}'}(-\partial f_0/\partial \mathcal{E}_{\boldsymbol{k}})(-\partial f_0/\partial \mathcal{E}_{\boldsymbol{k}'})}, \quad \text{(A31)}$$

where $N(0) \equiv \sum_{\boldsymbol{k}}(-\partial f_0/\partial \mathcal{E}_{\boldsymbol{k}})$ and the weighting factor $w_{\boldsymbol{k}\boldsymbol{k}'}$ is 1 for the single-particle scattering rate and $(v_{\boldsymbol{k}x} - v_{\boldsymbol{k}'x})^2$ for the transport scattering rate.

———————————

[1] K. G. Nazaryan and L. Levitov, *Robustness of vorticity in electron fluids*, arXiv:2111.09878.

[2] L. W. Molenkamp and M. J. De Jong, *Electron-electron-scattering-induced size effects in a two-dimensional wire*, Phys. Rev. B **49**, 5038 (1994).

[3] M. J. M. DeJong and L. W. Molenkamp, *Hydrodynamic electron flow in high-mobility wires*, Phys. Rev. B **51**, 13389 (1995).

[4] C. Q. Cook and A. Lucas, *Electron hydrodynamics with a polygonal Fermi surface*, Phys. Rev. B **99**, 235148 (2019).

[5] G. Varnavides, A. S. Jermyn, P. Anikeeva, C. Felser, and P. Narang, *Electron hydrodynamics in anisotropic materials*, Nat. Commun. **11**, 4710 (2020).

[6] C. Q. Cook and A. Lucas, *Viscometry of electron fluids from symmetry*, Phys. Rev. Lett. **127**, 176603 (2021).

[7] M. Qi and A. Lucas, *Distinguishing viscous, ballistic, and diffusive current flows in anisotropic metals*, Phys. Rev. B **104**, 195106 (2021).

[8] P. J. Turner, D. M. Broun, S. Kamal, M. E. Hayden, J. S. Bobowski, R. Harris, D. C. Morgan, J. S. Preston, D. A. Bonn, and W. N. Hardy, *Bolometric technique for high-resolution broadband microwave spectroscopy of ultra-low-loss samples*, Rev. Sci. Instrum. **75**, 124 (2004).

[9] W. A. Huttema, B. Morgan, P. J. Turner, W. N. Hardy, X. Zhou, D. A. Bonn, R. Liang, and D. M. Broun, *Apparatus for high-resolution microwave spectroscopy in strong magnetic fields*, Rev. Sci. Instrum. **77**, 023901 (2006).

[10] D. Bonn and W. Hardy, *Microwave Electrodynamics of High Temperature Superconductors*, in *Handbook of High-Temperature Superconductivity: Theory and Experiment*, edited by J. R. Schrieffer and J. S. Brooks (Springer, New York, 2007), pp. 145–214, 10.1007/978-0-387-68734-6_4.

[11] Y. Matsuda, N. P. Ong, Y. F. Yan, J. M. Harris, and J. B. Peterson, *Vortex viscosity in* YBa$_2$Cu$_3$O$_{7-\delta}$ *at low temperatures*, Phys. Rev. B **49**, 4380 (1994).

[12] J. C. Booth, D. H. Wu, and S. M. Anlage, *A broadband method for the measurement of the surface impedance of thin films at microwave frequencies*, Rev. Sci. Instrum. **65**, 2082 (1994).

[13] G. E. H. Reuter and E. H. Sondheimer, *The theory of the anomalous skin effect in metals*, Proc. R. Soc. A **195**, 336 (1948).

[14] R. Dingle, *The anomalous skin effect and the reflectivity of metals I*, Physica **19**, 311 (1953).

[15] Equation. (5) is the expression for a semi-infinite sample with specular electron scattering at the sample surface [13],

while the expression for diffuse sample scattering is given in eq. (A2). Regardless of boundary conditions, the point remains that R depends on the direction of the wave vector and is an integrated function of its magnitude.

[16] E. H. Sondheimer, *The theory of the anomalous skin effect in anisotropic metals*, Proc. R. Soc. A **224**, 260 (1954).

[17] A. Pippard, *The anomalous skin effect in anisotropic metals*, Proc. R. Soc. A **224**, 273 (1954).

[18] A. Pippard, *The surface impedance of superconductors and normal metals at high frequencies II. The anomalous skin effect in normal metals*, Proc. R. Soc. A **191**, 385 (1947).

[19] R. G. Chambers, *Anomalous skin effect in metals*, Nature (London) **165**, 289 (1950).

[20] R. G. Chambers, *The anomalous skin effect*, Proc. R. Soc. A **215**, 481 (1952).

[21] G. Smith, *Anomalous skin effect in bismuth*, Phys. Rev. **115**, 1561 (1959).

[22] R. N. Gurzhi, *Hydrodynamic effects in solids at low temperature*, Sov. Phys. Usp. **11**, 255 (1968).

[23] A. P. Mackenzie, R. K. Haselwimmer, A. W. Tyler, G. G. Lonzarich, Y. Mori, S. Nishizaki, and Y. Maeno, *Extremely strong dependence of superconductivity on disorder in* Sr$_2$RuO$_4$, Phys. Rev. Lett. **80**, 161 (1998).

[24] M. E. Barber, A. S. Gibbs, Y. Maeno, A. P. Mackenzie, and C. W. Hicks, *Resistivity in the vicinity of a van Hove singularity:* Sr$_2$RuO$_4$ *under uniaxial pressure*, Phys. Rev. Lett. **120**, 076602 (2018).

[25] See Supplemental Material at http://link.aps.org/supplemental/10.1103/PhysRevX.14.011018 for supporting information about the data analysis for our measurements on Sr$_2$RuO$_4$, Sn, and PdCoO$_2$, and a description of the parameters used for the temperature-dependent calculations shown in Fig. 6.

[26] N. Ashcroft and N. Mermin, *Solid State Physics* (Holt, Rinehart and Wilson, New York, 1976).

[27] C. W. Hicks, A. S. Gibbs, A. P. Mackenzie, H. Takatsu, Y. Maeno, and E. A. Yelland, *Quantum oscillations and high carrier mobility in the delafossite* PdCoO$_2$, Phys. Rev. Lett. **109**, 116401 (2012).

[28] V. Sunko, P. H. McGuinness, C. S. Chang, E. Zhakina, S. Khim, C. E. Dreyer, M. Konczykowski, H. Borrmann, P. J. W. Moll, M. König, D. A. Muller, and A. P. Mackenzie, *Controlled introduction of defects to delafossite metals by electron irradiation*, Phys. Rev. X **10**, 021018 (2020).

[29] P. J. W. Moll, P. Kushwaha, N. Nandi, B. Schmidt, and A. P. Mackenzie, *Evidence for hydrodynamic electron flow in* PdCoO$_2$, Science **351**, 1061 (2016).

[30] H.-J. Noh, J. Jeong, J. Jeong, E.-J. Cho, S. B. Kim, K. Kim, B. I. Min, and H.-D. Kim, *Anisotropic electric conductivity of delafossite* PdCoO$_2$ *studied by angle-resolved photoemission spectroscopy*, Phys. Rev. Lett. **102**, 256404 (2009).

[31] V. Sunko, H. Rosner, P. Kushwaha, S. Khim, F. Mazzola, L. Bawden, O. J. Clark, J. M. Riley, D. Kasinathan, M. W. Haverkort, T. K. Kim, M. Hoesch, J. Fujii, I. Vobornik, A. P. Mackenzie, and P. D. King, *Maximal Rashba-like spin splitting via kinetic-energy-coupled inversion-symmetry breaking*, Nature (London) **549**, 492 (2017).

[32] M. D. Bachmann, A. L. Sharpe, A. W. Barnard, C. Putzke, M. König, S. Khim, D. Goldhaber-Gordon, A. P. Mackenzie, and P. J. W. Moll, *Super-geometric electron focusing on the hexagonal Fermi surface of* PdCoO$_2$, Nat. Commun. **10**, 5081 (2019).

[33] P. H. McGuinness, E. Zhakina, M. König, M. D. Bachmann, C. Putzke, P. J. W. Moll, S. Khim, and A. P. Mackenzie, *Low-symmetry nonlocal transport in microstructured squares of delafossite metals*, Proc. Natl. Acad. Sci. U.S.A. **118**, e2113185118 (2021).

[34] M. D. Bachmann, A. L. Sharpe, G. Baker, A. W. Barnard, C. Putzke, T. Scaffidi, N. Nandi, P. H. Mcguinness, E. Zhakina, M. Moravec, S. Khim, M. König, D. Goldhaber-Gordon, A. P. Mackenzie, and P. J. W. Moll, *Directional ballistic transport in the two-dimensional metal* PdCoO$_2$, Nat. Phys. **18**, 819 (2022).

[35] U. Frisch, B. Hasslacher, and Y. Pomeau, *Lattice-gas automata for the Navier-Stokes equation*, Phys. Rev. Lett. **56**, 1505 (1986).

[36] A. Pippard, *An experimental determination of the Fermi surface in copper*, Phil. Trans. R. Soc. A **250**, 325 (1957).

[37] M. L. Glasser, *Influence of band structure on the nonlocal conductivity of metals and the anomalous skin effect*, Phys. Rev. **176**, 1110 (1968).

[38] M. I. Kaganov and P. Contreras, *Theory of the anomalous skin effect in metals with complicated Fermi surfaces*, J. Exp. Theor. Phys. **79**, 985 (1994).

[39] N. A. Zimbovskaya, *Local features of the Fermi surface curvature and the anomalous skin effect in metals*, J. Phys. Condens. Matter **18**, 8149 (2006).

[40] T. Harada, K. Fujiwara, and A. Tsukazaki, *Highly conductive* PdCoO$_2$ *ultrathin films for transparent electrodes*, APL Mater. **6**, 046107 (2018).

[41] M. Brahlek, G. Rimal, J. M. Ok, D. Mukherjee, A. R. Mazza, Q. Lu, H. N. Lee, T. Z. Ward, R. R. Unocic, G. Eres, and S. Oh, *Growth of metallic delafossite* PdCoO$_2$ *by molecular beam epitaxy*, Phys. Rev. Mater. **3**, 093401 (2019).

[42] J. Sun, M. R. Barone, C. S. Chang, M. E. Holtz, H. Paik, J. Schubert, D. A. Muller, and D. G. Schlom, *Growth of* PdCoO$_2$ *by ozone-assisted molecular-beam epitaxy*, APL Mater. **7**, 121112 (2019).

[43] Note that the convention for defining γ_{mc} that we have used here, following Ref. [44], differs from that used by Ref. [29]. The relationship between the two conventions is explained in Ref. [45]. In our convention, we infer $\gamma_{mc}/\gamma_{mr} = 7$, and Ref. [29] infers a value of 11. In the convention of Ref. [29], we infer a value of 6, and Ref. [29] infers a value of 10. Nonetheless, the value in Ref. [29] was stated as a rough estimate, and we have included an uncertainty of ± 3 in our determination so that the two inferences are close, relative to experimental uncertainty.

[44] D. Valentinis, G. Baker, D. A. Bonn, and J. Schmalian, *Kinetic theory of the non-local electrodynamic response in anisotropic metals: skin effect in 2D systems*, Phys. Rev. Res. **5**, 013212 (2023).

[45] G. Baker, D. Valentinis, and A. P. Mackenzie, *On non-local electrical transport in anisotropic metals*, Fiz. Nizk. Temp. **49**, 1475 (2023) [Low Temp. Phys. **49**, 1338 (2023)].

[46] Y. Wang, G. Varnavides, R. Sundararaman, P. Anikeeva, J. Gooth, C. Felser, and P. Narang, *Generalized design principles for hydrodynamic electron transport in anisotropic metals*, Phys. Rev. Mater. **6**, 083802 (2022).

[47] A. Aharon-Steinberg, T. Völkl, A. Kaplan, A. K. Pariari, I. Roy, T. Holder, Y. Wolf, A. Y. Meltzer, Y. Myasoedov, M. E. Huber, B. Yan, G. Falkovich, L. S. Levitov, M. Hücker, and E. Zeldov, *Direct observation of vortices in an electron fluid*, Nature (London) **607**, 74 (2022).

[48] R. N. Gurzhi, *Minimum of resistance in impurity-free conductors*, Sov. Phys. JETP **44**, 771 (1963).

[49] A. Levchenko and J. Schmalian, *Transport properties of strongly coupled electron–phonon liquids*, Ann. Phys. (N.Y.) **419**, 168218 (2020).

[50] X. Huang and A. Lucas, *Electron-phonon hydrodynamics*, Phys. Rev. B **103**, 155128 (2021).

[51] Even more dramatic ratios of the transport and single-particle times have been reported in the ultra-highconductivity semimetals Cd$_3$As$_2$ [T. Liang, Q. Gibson, M. N. Ali, M. Liu, R. J. Cava, and N. P. Ong, *Ultrahigh mobility and giant magnetoresistance in the Dirac semimetal* Cd$_3$As$_2$, Nat. Mater. **14**, 280 (2015)]; WP$_2$[N. Kumar, Y. Sun, N. Xu, K. Manna, M. Yao, V. Süss, I. Leermakers, O. Young, T. Förster, M. Schmidt, H. Borrmann, B. Yan, U. Zeitler, M. Shi, C. Felser, and C. Shekhar, *Extremely high magneto-resistance and conductivity in the type-II Weyl semimetals* WP$_2$ *and* MoP$_2$, Nat. Commun. **8**, 1642 (2017)]; Sb [A. Jaoui, A. Gourgout, G. Seyfarth, A. Subedi, T. Lorenz, B. Fauqué, and K. Behnia, *Formation of an electron-phonon bifluid in bulk antimony*, Phys. Rev. X **12**, 031023 (2022)]. However, in these systems other mechanisms may be involved, including suppression of backscattering due to topological matrix element effects.

[52] P. T. Coleridge, *Small-angle scattering in two-dimensional electron gases*, Phys. Rev. B **44**, 3793 (1991).

[53] S. Das Sarma and F. Stern, *Single-particle relaxation time versus scattering time in an impure electron gas*, Phys. Rev. B **32**, 8442 (1985).

[54] X. Hong, K. Zou, and J. Zhu, *Quantum scattering time and its implications on scattering sources in graphene*, Phys. Rev. B **80**, 241415(R) (2009).

[55] E. H. Hwang and S. Das Sarma, *Single-particle relaxation time versus transport scattering time in a two-dimensional graphene layer*, Phys. Rev. B **77**, 195412 (2008).

[56] After the submission of this paper, thorough chemical analysis of single crystals of PdCoO$_2$ was used by Ref. [57] to show explicitly that the high level of out-of-plane impurities hypothesized here and in Ref. [28] indeed exists.

[57] Y. Zhang, F. Tutt, G. N. Evans, P. Sharma, G. Haugstad, B. Kaiser, J. Ramberger, S. Bayliff, Y. Tao, M. Manno, J. Garcia-Barriocanal, V. Chaturvedi, R. M. Fernandes, T. Birol, W. E. Seyfried, Jr., and C. Leighton, *Crystal-chemical origins of the ultrahigh conductivity of metallic delafossites*, arXiv:2308.14257.

[58] In this section, we employ a shorthand bra-ket notation [45]. Explicitly, this notation has the meaning

$$\langle a|A|b \rangle = 2\sum_{\boldsymbol{kk'}}\left(-\frac{\partial f_0}{\partial \mathcal{E}_{\boldsymbol{k}}}\right)a_{\boldsymbol{k}}^* A_{\boldsymbol{kk'}} b_{\boldsymbol{k'}}$$

and

$$\langle a|b \rangle = 2\sum_{\boldsymbol{k}} \left(-\frac{\partial f_0}{\partial \mathcal{E}_{\boldsymbol{k}}} \right) a_{\boldsymbol{k}}^* b_{\boldsymbol{k}}$$

where f_0 is the Fermi-Dirac distribution function, $\mathcal{E}_{\boldsymbol{k}}$ the electronic dispersion, and the factor of 2 comes from spin degeneracy.

[59] R. Sarvari, *Impact of Size Effects and Anomalous Skin Effect on Metallic Wires as GSI Interconnects*, Ph.D. thesis, Georgia Institute of Technology (2008).

[60] H. B. G. Casimir and J. Ubbink, *The skin effect II. The skin effect at high frequencies*, Philips Tech. Rev. **28**, 300 (1967).

[61] D. Forcella, J. Zaanen, D. Valentinis, and D. van der Marel, *Electromagnetic properties of viscous charged fluids*, Phys. Rev. B **90**, 035143 (2014).

[62] D. Valentinis, J. Zaanen, and D. Van Der Marel, *Propagation of shear stress in strongly interacting metallic Fermi liquids enhances transmission of terahertz radiation*, Sci. Rep. **11**, 7105 (2021).

[63] D. Valentinis, *Optical signatures of shear collective modes in strongly interacting Fermi liquids*, Phys. Rev. Res. **3**, 023076 (2021).

[64] P. Matus, R. M. A. Dantas, R. Moessner, and P. Surówka, *Skin effect as a probe of transport regimes in Weyl semimetals*, Proc. Natl. Acad. Sci. U.S.A. **119**, e2200367119 (2022).

[65] We note that for an anisotropic Fermi surface, one must clarify what is meant by "momentum." Two obvious choices are the crystal momentum $\boldsymbol{k}$ and the expectation value $\langle \hat{\boldsymbol{p}} \rangle = m\boldsymbol{v}_{\boldsymbol{k}}$ of the momentum operator $\hat{\boldsymbol{p}} = (\hbar/i)\nabla$. In principle, the two are not equivalent for an anisotropic Fermi surface, and the subtleties of this distinction are beyond the scope of the present work [45]. In practice, both choices lead to similar numerical results for the surface resistance of $PdCoO_2$ with in-plane wave-vector direction, and the choice does not affect our conclusions. The results shown in the main text are based on taking $\boldsymbol{p}$ as $\langle \hat{\boldsymbol{p}} \rangle$.

[66] F. Stern, *Polarizability of a two-dimensional electron gas*, Phys. Rev. Lett. **18**, 546 (1967).

[67] C. M. Yim, D. Chakraborti, L. C. Rhodes, S. Khim, A. P. Mackenzie, and P. Wahl, *Quasiparticle interference and quantum confinement in a correlated Rashba spin-split 2D electron liquid*, Sci. Adv. **7**, eabd7361 (2021).

[68] P. B. Allen, *Boltzmann Theory and Resistivity of Metals*, in *Quantum Theory of Real Materials*, edited by J. R. Chelikowsky and S. G. Louie (Springer, New York, 1996), 1st ed., Chap. 17, pp. 219–250.